How coherent are the vortices of two-dimensional turbulence?

Mohammad Farazmand[1, 2] and George Haller[2]

[1)] *Department of Mathematics, ETH Zurich, Switzerland*

[2)] *Institute of Mechanical Systems, ETH Zurich, Switzerland*

(Dated: 21 February 2014)

We use recent developments in the theory of finite-time dynamical systems to objectively locate the material boundaries of coherent vortices in two-dimensional Navier–Stokes turbulence. We show that these boundaries are optimal in the sense that any closed curve in their exterior will lose coherence under material advection. Through a detailed comparison, we find that other available Eulerian and Lagrangian techniques significantly underestimate the size of each coherent vortex.

arXiv:1402.4835v1 [math.DS] 19 Feb 2014

I. INTRODUCTION

Coherent vortices are persistent patches of rotating fluid that are observed in experimentally and numerically generated two-dimensional turbulence (Kellay and Goldburg, 2002; Boffetta and Ecke, 2012). As opposed to a typical closed material line, the boundary of a coherent vortex is envisioned to preserve its overall shape without substantial stretching, folding or filamentation. While intuitive and simple, this material view on vortices is surprisingly challenging to formulate in rigorous and computable mathematical terms (Frisch, 1995; McWilliams, 2006).

For the detection of coherent vortices, the most natural quantity to consider is vorticity itself, which is almost invariant along fluid trajectories in high-Reynolds-number two-dimensional turbulence. Vorticity, however, can drastically differ in coordinate frames rotating relative to each other, resulting in conflicting vortex detections in different frames. Moreover, there are no well-justified thresholds over which a vortex contour could be considered coherent.

To circumvent the shortcomings of the vorticity field, a number of Eulerian scalar quantities have been developed for vortex detection (see Jeong and Hussain (1995) and Haller (2005) for a review). These methods attempt to quantify the rotation of fluid elements against the strain they experience. Simply connected regions with dominant rate of rotation are then defined as vortices. For instance, the Okubo-Weiss (OW) criterion (Okubo, 1970; Weiss, 1991) measures the difference between the instantaneous rates of rotation and strain assuming that these quantities evolve slowly in time. Later, Hua and Klein (1998) accounted for rapid changes in strain and rotation by including higher-order terms, i.e., acceleration terms.

In addition to their lack of objectivity, these Eulerian indicators are not ideal for coherent vortex detection because, unlike vorticity, they are not preserved along fluid trajectories. As a result, the detected vortex boundaries at different time instances do not evolve into each other when advected under the flow. This invariance under the flow map is desirable since our intuitive understanding of a coherent vortex as a rotating body of fluid is Lagrangian in nature.

A recent development in the theory of finite-time dynamical systems (Haller and Beron-Vera, 2013) offers an objective Lagrangian measure of coherence that can be applied to

coherent vortices of two-dimensional turbulence. Haller and Beron-Vera (2013) show that an appropriately defined Lagrangian strain energy necessarily vanishes along coherent (i.e., non-filamenting) material lines. They develop a numerical method based on this principle to find closed coherent material lines in two-dimensional flows, and apply it to satellite-derived surface velocities in the ocean.

Here, we use their method to detect the optimal boundaries of coherent vortices in a direct numerical simulation of Navier-Stokes turbulence. We also carry out a detailed comparison with alternative Eulerian and Lagrangian techniques. This comparison reveals that the coherent vortices that survive for long times are significantly larger than what has been thought so far.

In section §II, we use Lagrangian vortex detection method of Haller and Beron-Vera (2013) to locate vortices objectively in a direct numerical simulation of Navier–Stokes turbulence. We verify that the coherent vortex boundaries obtained in this fashion are indeed optimal. With these optimal boundaries at hand, we find that coherent vortices are significantly larger in enclosed surface area but also smaller in number than previously thought.

In Section §II, we briefly review the variational theory of Haller and Beron-Vera (2013). Our results are presented in Section §III. Section §IV contains our concluding remarks.

II. PRELIMINARIES

A. Set-up

Let $u(x,t)$ be a two-dimensional velocity field, defined over positions x in an open domain $U \subset \mathbb{R}^2$ and times t ranging though a finite interval $I = [a,b]$. The motion of passive fluid particles under such a velocity field is governed by the differential equation

$$\dot{x} = u(x,t), \tag{1}$$

where $x(t;t_0,x_0)$ is the position of a particle at time t whose initial position at time t_0 is $x_0 \in U$. For the fixed time interval I, the dynamical system (1) defines the specific flow map

$$\begin{aligned} F : U &\to U \\ x_a &\mapsto x_b, \end{aligned} \tag{2}$$

that takes an initial condition x_a to its time-b position $x_b = F(x_a) := x(b;a,x_a)$.

B. Coherence principle

A typical set of fluid particles deforms significantly as advected under the flow map F, provided that the advection time $b-a$ is at least of the order of a few eddy turn-over times in a turbulent flow (Aref, 1984). One may seek coherent material vortices as atypical sets of fluid trajectories that defy this trend by preserving their overall shape. These shapes are necessarily bounded by closed material lines that rotate and translate, but otherwise show no appreciable stretching or folding.

Haller and Beron-Vera (2013) seek Lagrangian vortex boundaries as closed material lines exhibiting no leading order average straining. A thin material belt around a typical material line γ experiences visible straining as advected under the flow. The material belt around a coherent material line, however, does not exhibit any noticeable strain (see figure 1).

To formulate this mathematically, let γ be a closed material line over the time interval $[a,b]$ and let $r : s \mapsto r(s)$ be a parametrization of γ at the initial time $t=a$. The *averaged tangential strain* of this material line over the time interval $I=[a,b]$ is then given by

$$Q(\gamma) = \frac{1}{\sigma}\int_0^\sigma \frac{\sqrt{\langle r'(s), C(r(s))r'(s)\rangle}}{\sqrt{\langle r'(s), r'(s)\rangle}}\mathrm{d}s, \tag{3}$$

where $s \in [0,\sigma]$. The Cauchy–Green strain tensor $C = DF^\top DF$ is defined in terms of the Jacobian of the flow map DF with the symbol $\top$ denoting matrix transposition (Truesdell and Noll, 2004). The *prime* denotes the derivative with respect to the arc-length s and $\langle\cdot,\cdot\rangle$ denotes the Euclidean inner product.

Consider a small perturbation to γ given by $\gamma+\epsilon h$ where $0<\epsilon\ll 1$ and $h:[0,\sigma]\to\mathbb{R}^2$ is a σ-periodic $\mathcal{O}(1)$ vector field orthogonal to γ. The perturbation $\gamma+\epsilon h$ represents the thin material belt of figure 1. For a typical material line, we have $Q(\gamma+\epsilon h) = Q(\gamma)+\mathcal{O}(\epsilon)$ due to the smoothness of the flow map F. That is $\mathcal{O}(\epsilon)$-perturbations to the material line γ lead to a $\mathcal{O}(\epsilon)$-perturbation in the averaged tangential strain Q. Haller and Beron-Vera (2013) argue that for a thin material belt centered on γ to remain coherent, it should not exhibit a leading-order change in its averaged straining. The leading order is meant with respect to the width of the material belt. In other words, $Q(\gamma+\epsilon h) = Q(\gamma)+\mathcal{O}(\epsilon^2)$ for a coherent material line γ, that is the first variation of Q vanishes: $\delta Q(\gamma)=0$.

The Euler-Lagrange equations arising from the condition $\delta Q(\gamma)=0$ are too complicated to yield any insight. Haller and Beron-Vera (2013) show, however, that a material line

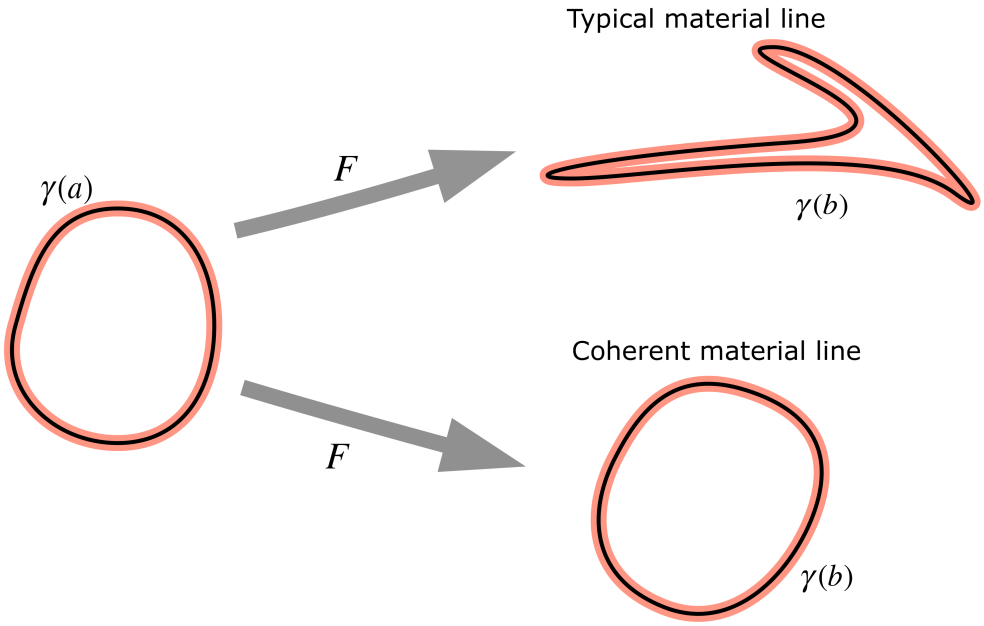

FIG. 1: Deformation of a typical material line γ versus a coherent material line as advected under the flow map F from time $t = a$ to $t = b$. No leading-order straining is observed in the material belt (red) around a coherent material line.

satisfies $\delta Q(\gamma) = 0$ if and only if it satisfies the pointwise condition

$$\langle r'(s), E_\lambda(r(s))r'(s)\rangle = 0, \tag{4}$$

for some constant $\lambda > 0$. The generalized *Green–Lagrange strain tensor* E_λ in (4) is defined in terms of the *Cauchy–Green strain tensor* C as

$$E_\lambda = \frac{1}{2}[C - \lambda^2 I], \tag{5}$$

where I is the two-by-two identity matrix.

Solving the implicit differential equation (4) simplifies locating coherent material lines as it has the explicit solutions

$$r' = \eta_\lambda^{\pm}(r) := \sqrt{\frac{\lambda_2(r) - \lambda^2}{\lambda_2(r) - \lambda_1(r)}}\xi_1(r) \pm \sqrt{\frac{\lambda^2 - \lambda_1(r)}{\lambda_2(r) - \lambda_1(r)}}\xi_2(r), \tag{6}$$

in terms of the invariants of the Cauchy–Green strain tensor C: $0 < \lambda_1 \leq \lambda_2$ are eigenvalues of C and $\{\xi_1, \xi_2\}$ are their corresponding eigenvectors. In an incompressible flow, $\lambda_1\lambda_2 = 1$ (Arnold, 1978).

The vectors η_λ^+ and η_λ^- are one-parameter families of vector fields with λ being the parameter. In an incompressible flow, we have $\lambda_2 \geq 1$ and $\lambda_1 \leq 1$. Therefore, for $\lambda = 1$, $\eta_\lambda^\pm$ are well-defined real vector fields over the entire physical domain U. For $\lambda \neq 1$, the vector fields $\eta_\lambda^\pm$ are only defined over a subset $U_\lambda \subset U$ where $\lambda_2 \geq \lambda^2$ and $\lambda_1 \leq \lambda^2$. The trajectories of $\eta_\lambda^\pm$ can be computed over U_λ. We refer to these trajectories as λ-stretching material lines (or λ-*lines*, for short)

C. Lagrangian vortex boundaries and λ-lines

Here, we discuss some properties of the λ-lines that are of relevance for the Lagrangian coherent vortex detection in two-dimensional turbulence.

(i) *Uniform stretching*: λ-lines stretch uniformly by a factor of λ as advected under the flow map F. To quantify this statement, let γ_a be time-a position of a λ-line parametrized by $r : s \mapsto r(s)$. Since γ_a is a λ-line, we have $r'(s) \parallel \eta_\lambda^\pm(r(s))$. Its time-$b$ position γ_b will be parametrized by $F \circ r : s \mapsto F(r(s))$ whose tangential vector is given by $DF(r(s))r'(s)$. It is readily verifiable that $|DF(r(s))r'(s)| = \lambda|r'(s)|$. That is each material element of γ_a stretches by a factor of λ as advected by the flow to time $t = b$. Consequently, the total length of the curve changes by a factor of λ, i.e. $\ell(\gamma_b) = \lambda\ell(\gamma_a)$, where ℓ is the length of the curve.

For $\lambda = 1$, this implies that the final length $\ell(\gamma_b)$ is equal to the initial length $\ell(\gamma_a)$ and therefore the material line is, in fact, *non-stretching*. This is an atypical behavior for a material line in a turbulent flow, as a typical material line will stretch (or shrink) significantly under advection. This, however, does *not* imply unlikelihood of the existence of non-stretching material lines. In fact, through any point in the domain U there are two such material lines computable as the solution curves of η_1^+ and η_1^-.

For $\lambda \neq 1$, a similar statement holds for the subset $U_\lambda \subset U$: Passing through any point in U_λ are two uniformly stretching material lines that stretch by a factor λ.

(ii) *Existence of closed λ-lines*: Although λ-lines fill the set U_λ densely, they tend to be typically open. In general, the existence of closed λ-lines depends on the dynamical system. As shown in section §III, closed λ-lines exist in two-dimensional turbulent flows and mark the boundaries of coherent vortices. In fact, closed λ-lines always appear as a nested family of curves corresponding to different λ values close to 1 (Haller and Beron-Vera, 2013).

(iii) *Relation to Lagrangian vortex boundaries*: Why should one expect the Lagrangian vortex boundaries to be marked by closed λ-lines? In an incompressible flow, the area enclosed by any closed curve is invariant under the flow map (Arnold, 1978). Closed λ-lines with $\lambda = 1$, in addition, preserve their arc-length. As a consequence of this dual invariance of enclosed area and arc-length, closed λ-lines cannot deform significantly as advected under the flow map F. This property is the hallmark of coherent vortex boundaries in two-dimensional turbulence.

(iv) *Relation to KAM tori*: In time-periodically perturbed two-dimensional Hamiltonian systems, Kolmogorov-Arnold-Moser (KAM) curves are material lines that return onto themselves after some time-period of the perturbation (Guckenheimer and Holmes, 1983). As a result, KAM curves encircle regions with coherent dynamics, usually referred to as elliptic regions. In a temporally aperiodic system, however, material lines are generally not expected to come back on themselves at any time instance. Yet, elliptic regions with coherent dynamics are known to exist even in complex, aperiodic dynamical systems such as two-dimensional turbulence. Closed λ-lines are, in this sense, the generalization of the KAM curves to aperiodic flows. In the periodic case, it has been shown that KAM curves coincide with closed λ-lines (Haller and Beron-Vera, 2012; Hadjighasem et al., 2013).

In light of the above discussion, we will seek Lagrangian coherent vortex boundaries as closed λ-lines. We refer to closed λ-lines as *elliptic Lagrangian coherent structures* (or elliptic LCSs, for short). In the case $\lambda = 1$, they are referred to as *primary* elliptic LCSs.

D. Black-hole analogy

As pointed out in Haller and Beron-Vera (2013), elliptic LCSs are analogous to black holes in cosmology. Over the subset U_λ of the flow domain, the bilinear form $g_\lambda : \mathbb{R}^2 \times \mathbb{R}^2 \to \mathbb{R}$ given by

$$g_\lambda(v, w) = \langle v, E_\lambda w \rangle,$$

defines a Lorentzian metric with signature $(-, +)$. (U_λ, g_λ) is a two-dimensional Lorentzian manifold. This manifold is similar to the space-time continuum in general relativity. In that context the manifold (U_λ, g_λ) is referred to as a two-dimensional space-time. Note that as opposed to Euclidean geometry, the distance between two distinct points measured by a

Lorentzian metric can be negative or zero.

In the space-time geometry, light travels along null-geodesics of the metric g_λ which coincide with the λ-lines defined above. Near a black hole, the gravity is strong enough to trap the light on a closed orbit called a *photon sphere* (Beem et al., 1996). Therefore, elliptic LCSs and hence Lagrangian vortex boundaries are the fluid analogs of photon spheres.

III. RESULTS AND DISCUSSION

We will use the method described in section §II to identify coherent Lagrangian vortices in a direct numerical simulation of two-dimensional forced turbulence.

A. Numerical method

Consider the Navier–Stokes equations

$$\partial_t u + u \cdot \nabla u = -\nabla p + \nu \Delta u + f, \tag{7a}$$

$$\nabla \cdot u = 0, \tag{7b}$$

$$u(x, 0) = u_0(x), \tag{7c}$$

where the velocity field $u(x, t)$ is defined on the two-dimensional domain $U = [0, 2\pi] \times [0, 2\pi]$ with doubly periodic boundary conditions.

We use a standard pseudo-spectral method with 512 modes in each direction and 2/3 dealiasing to solve the above Navier–Stokes equation with viscosity $\nu = 10^{-5}$. The time integration is carried out over the interval $t \in [0, 50]$ (approximately, three eddy-turn-over times) by a fourth-order Runge-Kutta method with variable step-size (Dormnad and Prince, 1980). The initial condition u_0 is the velocity field of a decaying turbulent flow. The external force f is random in phase and band-limited, acting on the wave-numbers $3.5 < k < 4.5$. The forcing amplitude is time-dependent balancing the instantaneous enstrophy dissipation $\nu \int k^2 Z(k, t)\, \mathrm{d}k$ where $Z(k, t) := \frac{1}{2} \int_{|\mathbf{k}|=k} |\hat{\omega}(\mathbf{k}, t)|^2\, \mathrm{d}S(\mathbf{k})$ with $\hat{\omega}(\cdot, t)$ being the Fourier transform of the instantaneous vorticity $\omega(\cdot, t) = \nabla \times u(\cdot, t)$.

In two dimensions, the energy injected into the system by the forcing is mostly transferred to larger scales through a nonlinear process (Kraichnan, 1967; Merilees and Warn, 1975). In order to prevent the energy accumulation at largest available scales over time, a linear

damping is usually added to the Navier–Stokes equation to dissipate the energy at large scales (Boffetta et al., 2002; Tsang et al., 2005). However, for the time scales considered here, the energy accumulation is not an issue and hence the linear damping will be omitted.

The theory reviewed in Section §II does not assume a particular governing equation for the velocity field $u(x,t)$. Thus, it can be applied to any two-dimensional velocity field, given as numerical solution of a partial differential equation or by direct measurements. In particular, it can be applied to Lagrangian vortex detection for the solutions of the Navier–Stokes equation (7). To detect the Lagrangian vortex boundaries, we take the following steps:

1. Solve the Navier–Stokes equation (7) as discussed above to get the velocity field $u(x,t)$ over the time interval $t \in [0, 50]$ and a uniform 512×512 spatial grid over the domain $x \in U = [0, 2\pi] \times [0, 2\pi]$. The temporal resolution of the velocity field is 251 such that two consecutive time slices are $\Delta t = 0.2$ apart.

2. Advect each grid point according to the differential equation (1) from time $t = 0$ to time $t = 50$ to construct the flow map F such that $F(x_a) = x_b$ for any grid point x_a.

3. Construct an approximation of the flow map gradient DF by finite differences. To increase the finite difference accuracy, we use the auxiliary grid method introduced in Farazmand and Haller (2012). The chosen auxiliary grid distance is 10^{-3}.

4. Construct the Cauchy–Green strain tensor $C(x_a) = [DF(x_a)]^\top DF(x_a)$ for each grid point x_a. Compute the eigenvalues $\{\lambda_1, \lambda_2\}$ and the corresponding eigenvectors $\{\xi_1, \xi_2\}$ of the Cauchy–Green strain tensor.

5. Seek the closed orbits of the one-parameter families of vector fields $\eta_\lambda^\pm$ defined in (6). For detecting these closed orbits, we use the automated algorithm developed in Haller and Beron-Vera (2013).

We detect the Lagrangian vortex boundaries as elliptic LCSs, i.e., the closed orbits of $\eta_\lambda^\pm$. In the following, we present a detailed analysis of these vortex boundaries and their relation to alternative Eulerian and Lagrangian indicators.

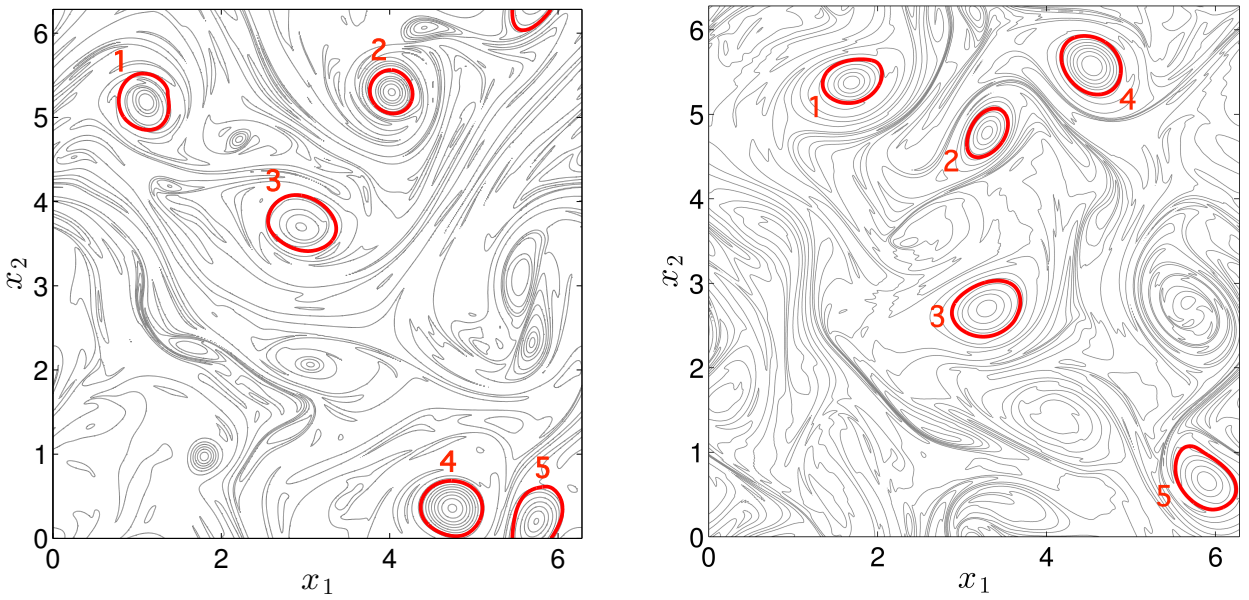

(a) (b)

FIG. 2: Lagrangian vortex boundaries (red) at time $t = 0$ (a) and $t = 50$ (b). The vorticity contours are shown in gray in the background. The vorticity contours are distributed as $-1 : 0.1 : 1$ at time $t = 0$ and as $-1.5 : 0.15 : 1.3$ at time $t = 50$. The coherent vortices are numbered in order to facilitate their identification at the two time-instances.

B. Lagrangian coherent vortex analysis

Figure 2a shows the boundaries (red) of Lagrangian coherent vortices superimposed on the contours of the Eulerian vorticity (gray) at time $t = 0$. The boundaries are found as the outermost elliptic LCSs, i.e., closed orbits of the vector fields $\eta_\lambda^\pm$ (see Eq. (6)). The advected image of the coherent vortex boundaries at time $t = 50$ are shown in figure 2b along with the corresponding instantaneous vorticity field. These coherent vortex boundaries resist straining and filamentation as advected under the flow. In the following, the vortex numbers refer to the numbering in figure 2.

Figure 3 shows the relative stretching $\delta\ell(t) := (\ell(t) - \ell(a))/\ell(a)$ of the primary elliptic LCSs over the time interval $t \in [0, 50]$. Here, $\ell(t)$ denotes the length of a material line at time t. In principle, the initial and the final lengths of a primary elliptic LCS must be exactly equal resulting in zero relative stretching at time $t = 50$. In practice, a deviation of at most 4% is observed from this ideal limit which arises from numerical errors. The inset of

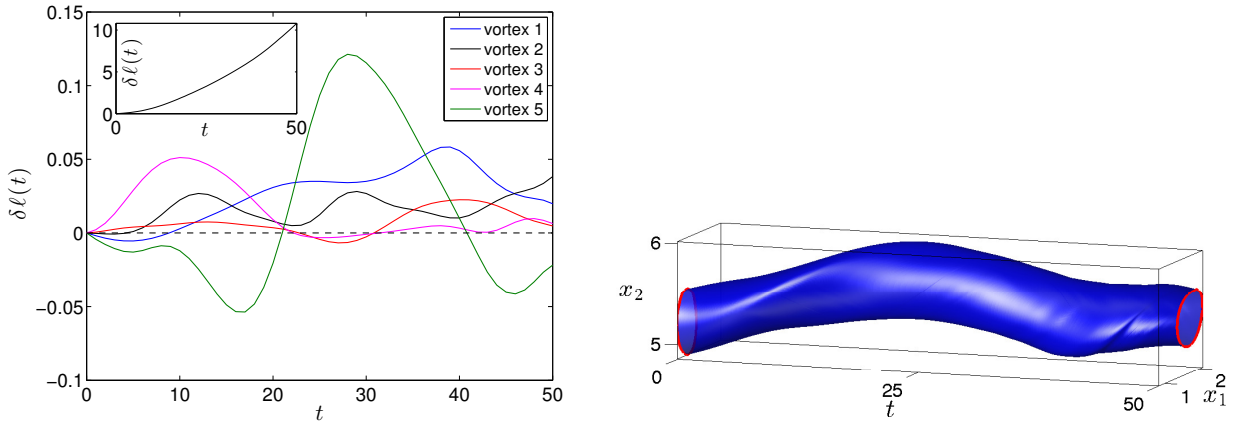

(a) (b)

FIG. 3: (a) The relative deformation as a function of time for the primary elliptic LCSs. The inset shows the relative stretching for a typical closed material line over the same time interval. (b) The Lagrangian vortex 1 in the extended phase space. The tube is created from the advection of the vortex boundary under the flow.

figure 3 shows the relative stretching of a typical non-coherent iso-vorticity line. Unlike the coherent vortices, the relative stretching for a general material curve increases exponentially, with its final value at least an order of magnitude larger than that of a coherent vortex.

As mentioned in section §II, coherent material vortex boundaries are formed by a nested set of elliptic LCSs (i.e., closed λ-lines). Figure 4 shows two of the coherent vortices and their corresponding λ-lines. We find that for vortex 1, the secondary elliptic LCSs with $\lambda > 1$ lie in the interior of the primary elliptic LCS (i.e., the closed λ-line with $\lambda = 1$). For all other coherent vortices of figure 2, the secondary elliptic LCSs with $\lambda > 1$ lie in the exterior of the primary elliptic LCS. In all five cases, values of λ for which an elliptic LCS exists are close to 1, ranging in the interval $0.94 \leq \lambda \leq 1.05$.

The majority of vortices appearing in figure 2a are not coherent in the Lagrangian frame, and hence no elliptic LCSs were found around them. Some of the non-coherent vortices are trapped in a hyperbolic region and experience substantial straining over time. Some others undergo a merger process where a larger vortex is created from two smaller co-rotating vortices. Each smaller vortex deforms substantially during the merger. The merged vortex may or may not remain coherent for later times.

Figure 5 focuses on one Eulerian vortex undergoing a merger process. To illustrate the

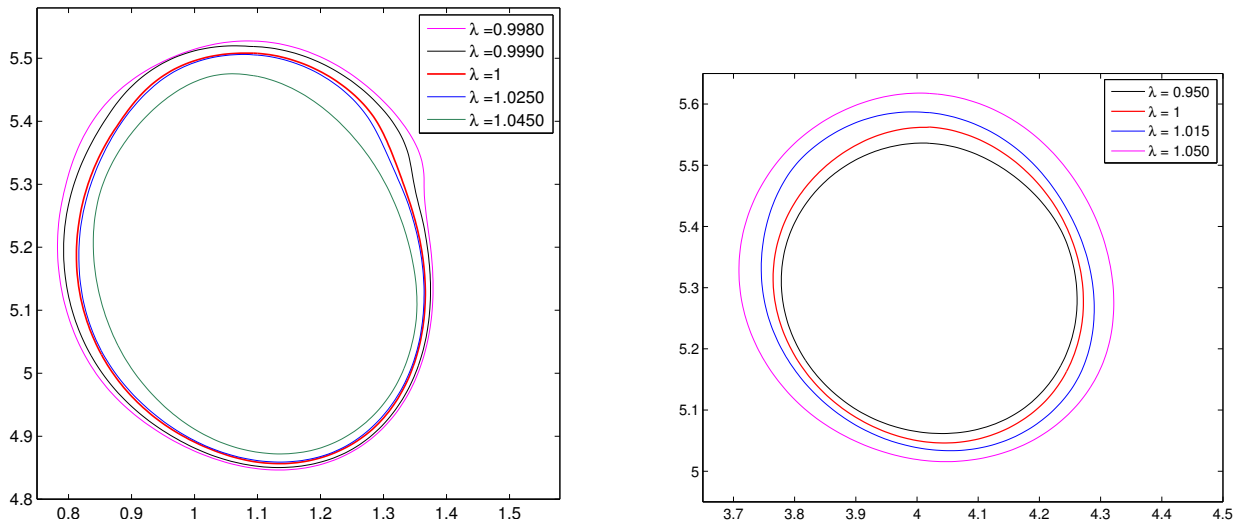

(a) (b)

FIG. 4: Elliptic LCSs (i.e., closed λ-lines) around vortex 1 (a) and vortex 2 (b).

deformation of this vortex, we take three vorticity contours at time $t = 0$ near the center of the vortex. Selected vorticity contours are then advected to the final time $t = 50$, showing the resulting deformation of the vortex core. Figure 6 shows a similar analysis for a non-coherent vortex trapped in a uniformly hyperbolic region of the flow. Hyperbolicity produces stretching of vorticity gradients resulting in smearing of the vortex.

Figure 7 shows the generalized stable and unstable manifolds obtained by the geodesic theory of Lagrangian coherent structures (Haller and Beron-Vera, 2012; Farazmand et al., 2013), using the computational method described in Farazmand and Haller (2013). These stable and unstable manifolds are, respectively, the most repelling and attracting material lines that form the skeleton of turbulent mixing patterns. The exponential attraction and repulsion generated by these manifolds leads to smearing of most fluid regions that appear as vortices in instantaneous streamline and vorticity plots. By contrast, coherent vortices we identify remain immune to extensive straining.

C. Optimality of coherent vortex boundaries

Here we consider the optimality of vortex boundaries obtained as outermost elliptic LCSs. The optimal boundary of a coherent vortex can be defined as a closed material line that encircles the largest possible area around the vortex and shows no filamentation over the

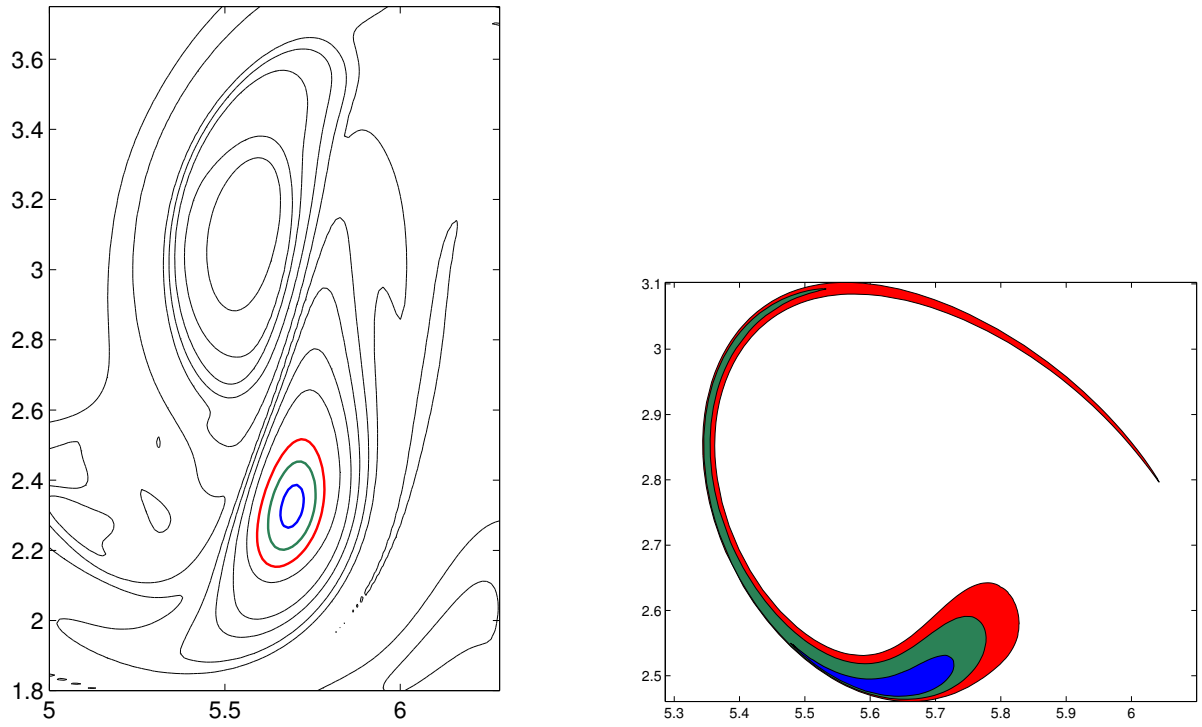

(a) (b)

FIG. 5: (a) Vortex contours at $t = 0$ for two non-coherent vortices that merge as one later in time. To demonstrate the deformation of the vortices we monitor the advection of three vorticity contours. The contour values are 0.6 (red), 0.7 (green) and 0.8 (blue). (b) The selected contours advected to time $t = 50$ and filled with their corresponding color.

observational time period. We seek to illustrate that outermost elliptic LCSs mark such optimal boundaries.

To this end, we considered a class of perturbations to the outermost elliptic LCS of vortex 1 corresponding to $\lambda = 0.998$. The perturbations are in the direction of the outer normal of the elliptic LCS. The amount of perturbation ranges between 0.01 and 0.06 (i.e., 1.5% to 10% of the diameter of the elliptic LCS). We then advect the vortex boundary and its perturbations to the final time $t = 50$ (see figure 8b). The perturbed curves visibly depart from the coherent core marked by the red elliptic LCS. Our findings are similar for all other coherent vortices (not shown here).

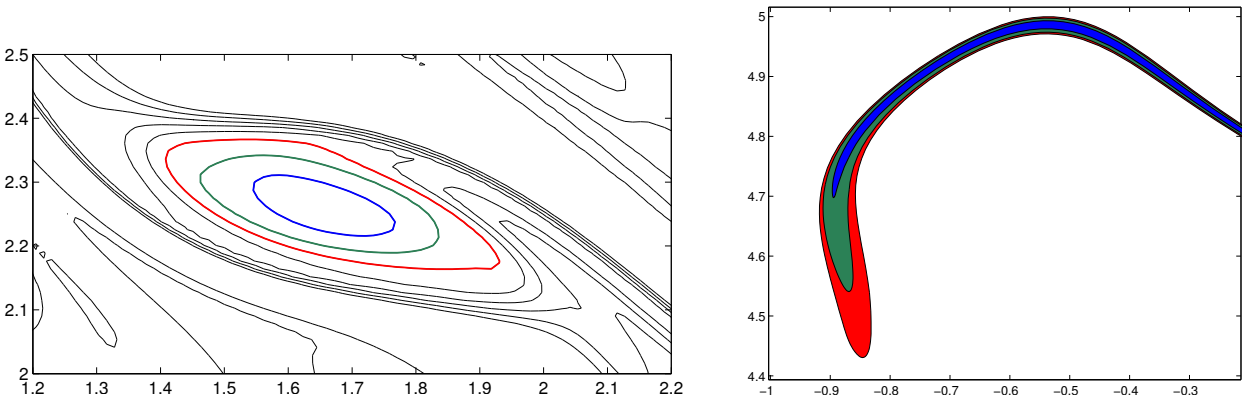

(a) (b)

FIG. 6: (a) Vortex contours at $t = 0$ for a non-coherent vortex trapped in a straining field. The contours of vorticity with values 0.25 (red), 0.3 (green) and 0.35 (blue) are marked. (b) The selected contours advected to time $t = 50$ and filled with their corresponding color. Only part of the advected image is shown.

D. Comparison with Eulerian and Lagrangian vortex indicators

There are several indicators that have been previously developed to mark vortex boundaries. Among the Eulerian indicators are vorticity criterion of McWilliams (1990), Okubo-Weiss (OW) criterion (Okubo, 1970; Weiss, 1991) and the modified OW criterion of Hua and Klein (1998), to name a few. These Eulerian methods are instantaneous in nature and cannot be expected to capture long-term coherence in the Lagrangian frame. Nevertheless, they are broadly believed to be good first-order indicators of coherence in the flow.

We find that the coherent vortex boundaries obtained as outermost elliptic LCSs cannot be approximated by the instantaneous vorticity contours at the initial time $t = 0$. Figure 9 compares these vortex boundaries with the vorticity contours for two of the coherent vortices. None of the vorticity contours approximates the actual observed coherent vortex boundary of the Lagrangian frame. In fact, the nearby vorticity contours are not axisymmetric, even though that is intuitively expected for a vortex boundary (McWilliams, 1990). For instance, we mark the closest contour to the elliptic LCS in blue which notably lacks axisymmetry. Its advected image at time $t = 50$ develops filaments. On the other hand, the magenta-colored axisymmetric contour closest to the elliptic LCS preserves its overall shape. This contour would, however, significantly underestimate the true extent of the coherent fluid region.

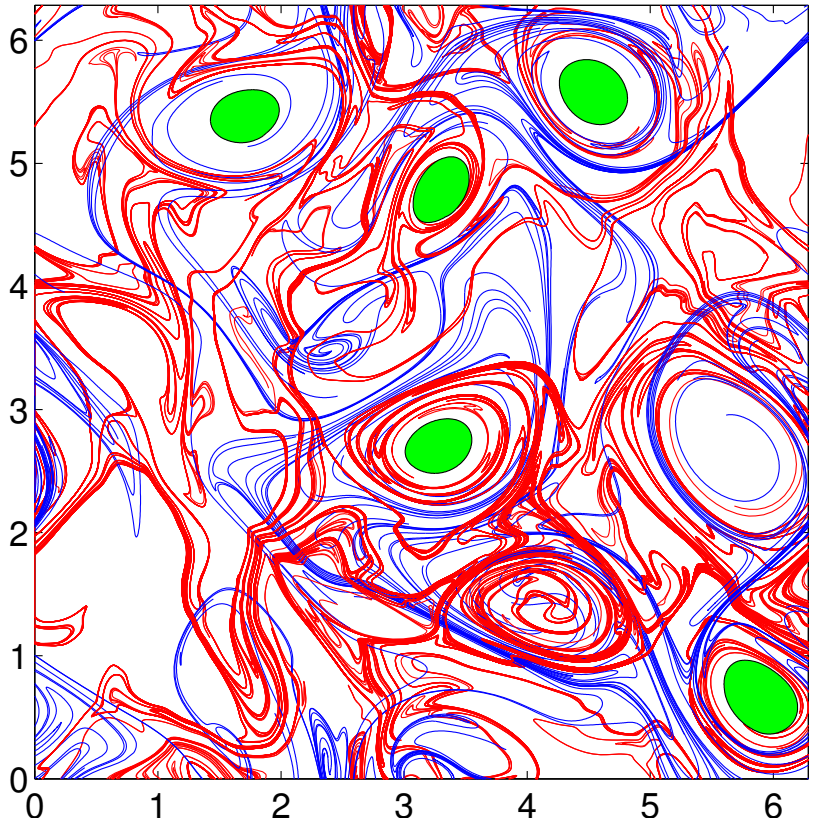

FIG. 7: Generalized stable (red) and unstable (blue) manifolds. The coherent Lagrangian vortices (green), i.e. generalized KAM regions, are not penetrated by these manifolds. The manifolds and the KAM regions are shown at $t = 50$.

Similar observations can be made for the OW criterion. The OW parameter

$$Q = \frac{1}{2}\left(|S|^2 - |\Omega|^2\right), \tag{8}$$

measures instantaneous straining against instantaneous rotation. Here, S and Ω are, respectively, the symmetric and anti-symmetric parts of the velocity gradient ∇u. The subset of the domain where $Q > 0$ is dominated by strain, while $Q < 0$ marks the regions dominated by vorticity. As a result, the zero contour of this parameter encircling a vortex may be expected to mark the outermost boundary of the vortical region. It has been pointed out by several authors (see, e.g., Pierrehumbert and Yang (1993)), however, that the zero contours of Q will not necessarily mark vortex-like structures.

We also find that the outermost elliptic LCS marking the observed material boundary of a coherent vortex is not approximated by the zero contour of the OW parameter. In fact, none of the OW contours approximate well the true coherent vortex boundary (see figure 10).

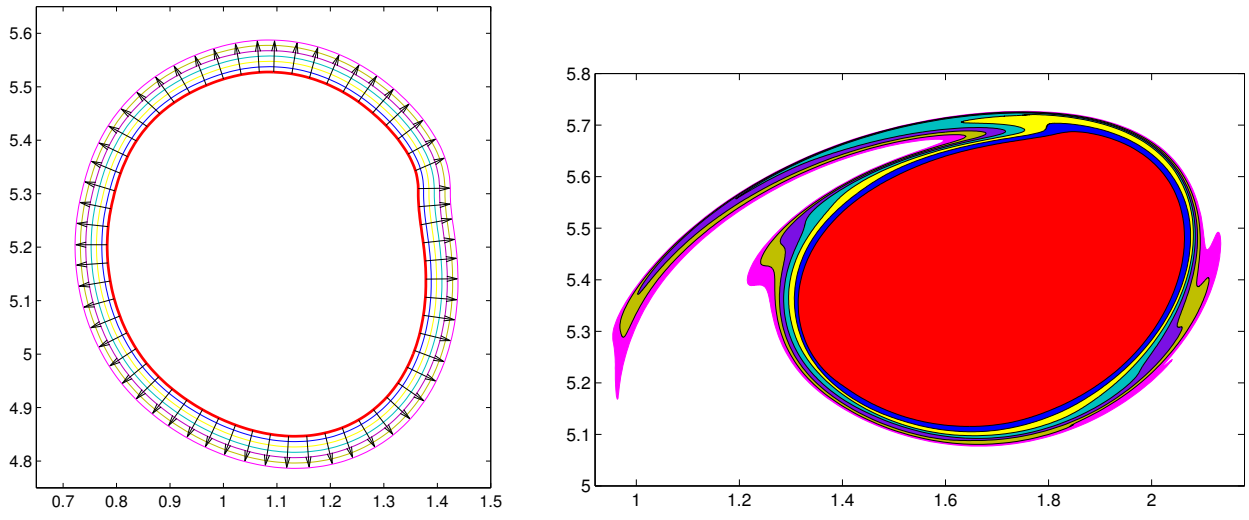

(a) (b)

FIG. 8: (a) The outermost elliptic LCS (red) encircling vortex 1 of figure 2 and its outer normal perturbations. The perturbation parameter ranges between 0.01 and 0.06. (b) The advected image of the elliptic LCS and its normal perturbations at time $t = 50$. Each advected image is filled with its corresponding color from panel (a)

The closest OW contour (blue curve) to the outermost elliptic LCS lacks axisymmetry and develops substantial filamentation under advection. The axisymmetric contour (magenta curve) contained in the coherent vortex preserves its shape but seriously underestimates the extent of the coherent region (as do axisymmetric vorticity contours). This axisymmetric contour of the OW parameter is also the outermost contour that remains in the $Q < 0$ region over the entire time interval $t \in [0, 50]$.

We make a similar observation about other OW-type Eulerian indicators that have been developed to overcome the shortcomings of the OW criterion (see, e.g., Chong et al. (1990); Tabor and Klapper (1994); Kida and Miura (1998); Hua and Klein (1998)).

Hua and Klein (1998), for instance, consider the effect of higher-order terms due to fluid acceleration. They arrive at the indicator parameters $\lambda_\pm$ given by

$$\lambda_\pm = Q \pm \sqrt{|\dot{S}|^2 - |\dot{\Omega}|^2},$$

where $\dot{S}$ and $\dot{\Omega}$ denote, respectively, the instantaneous rate of change of strain and vorticity along fluid trajectories. The scalar Q is the OW parameter, defined in (8). The positive extrema of λ_+ correspond to regions of instantaneously strong stirring and dispersion. The

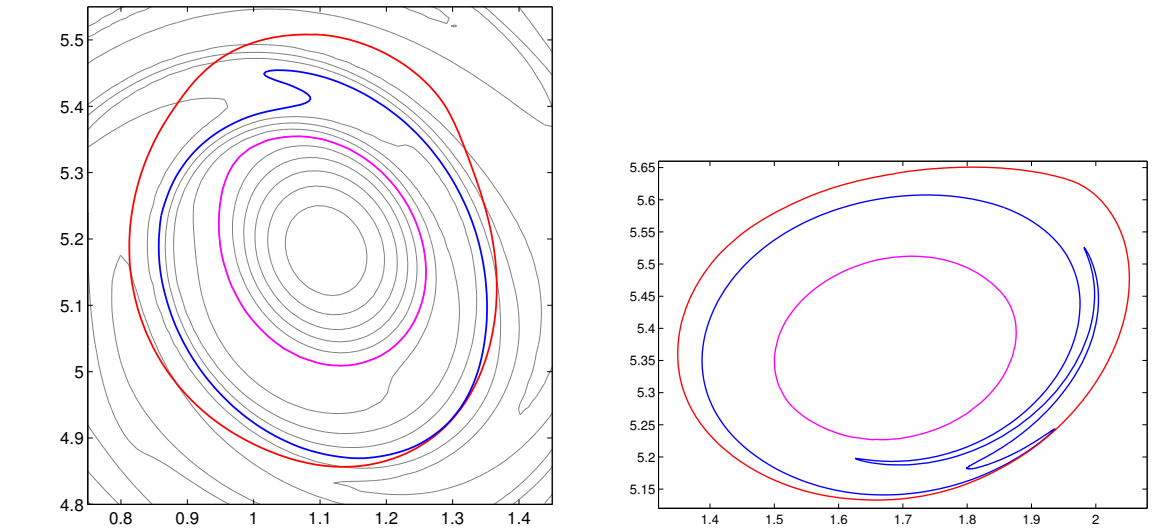

(a)

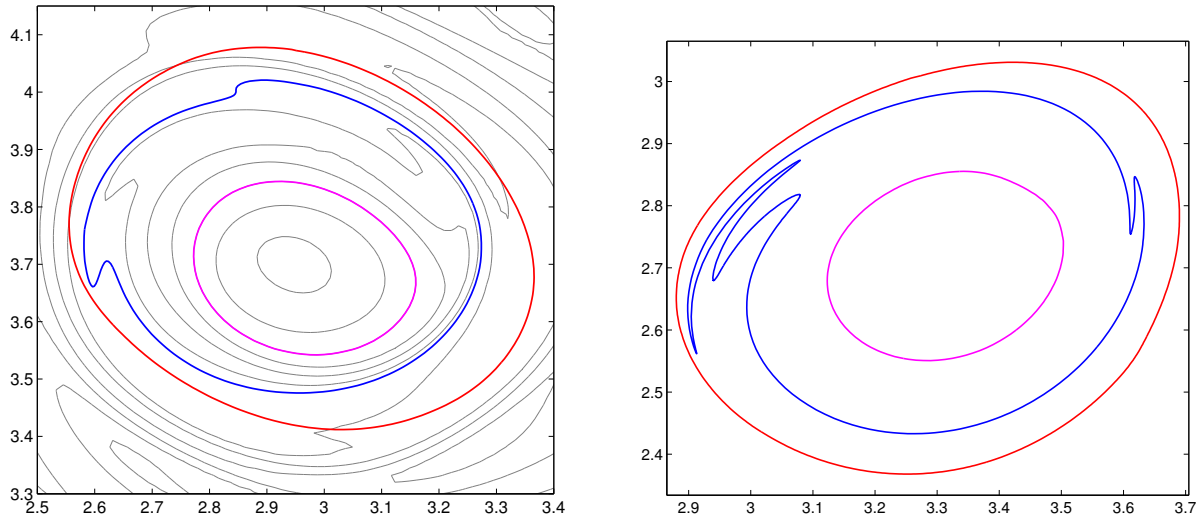

(b)

FIG. 9: (a) Left: Vorticity contours (gray) and the Lagrangian vortex boundary (red) for vortex 1 at time $t = 0$. The blue curve marks the closed vorticity contour that lays entirely inside the elliptic LCS. This contour corresponds to $\omega = -0.3$. The magenta curve marks the closest axisymmetric vorticity contour to the elliptic LCS. Right: The Lagrangian vortex boundary and selected vorticity contours advected to time $t = 50$. (b) Same as (a) for vortex 3. The contour marked by the blue curve corresponds to $\omega = -0.32$.

negative extrema of λ_-, on the other hand, mark the vortex regions.

As in the case of vorticity and the OW-parameter, we find that the Lagrangian vortex boundaries cannot be inferred from the contours of the $\lambda_\pm$ parameters (see figure 11). The

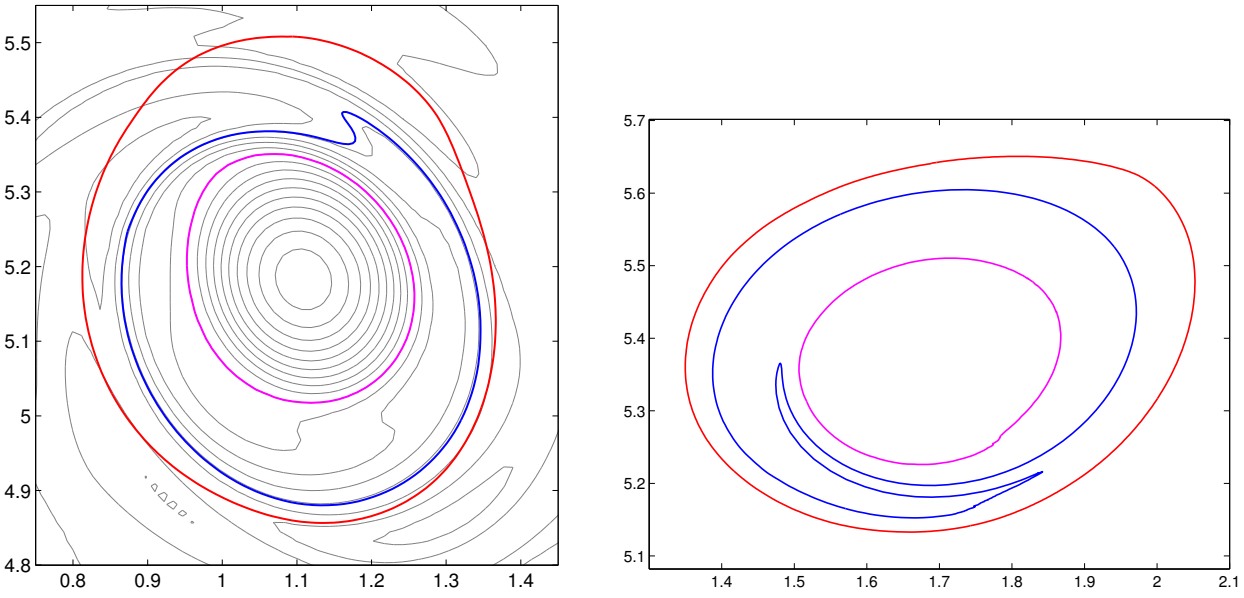

(a)

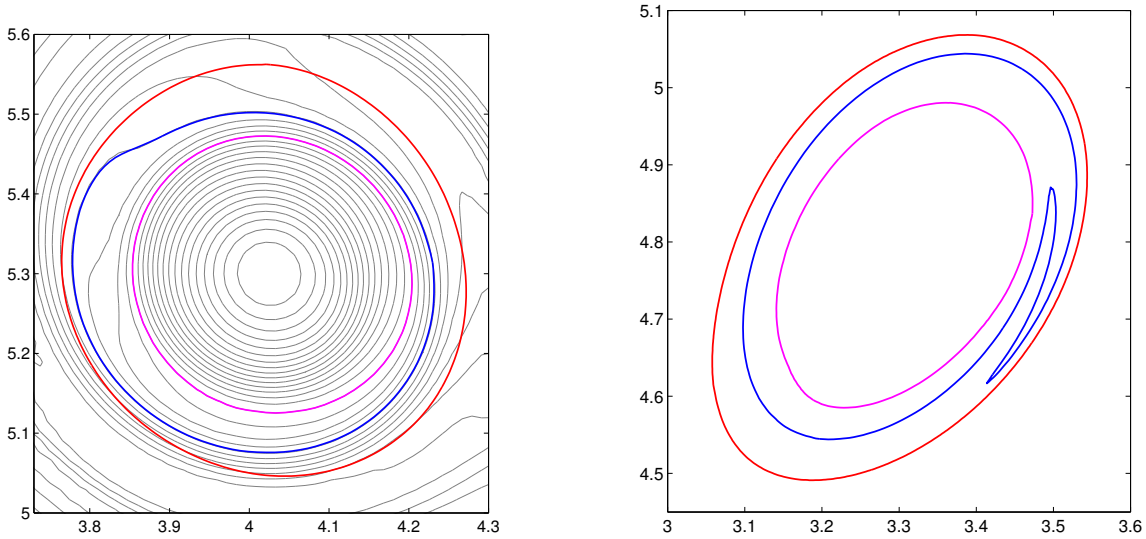

(b)

FIG. 10: (a) Left: OW contours (gray) and the Lagrangian vortex boundary (red) for vortex 1 at time $t = 0$. Two contours corresponding to $Q = -0.018$ (blue) and $Q = -0.06$ (magenta) are selected for advection. Right: The Lagrangian vortex boundary and selected OW contours advected to time $t = 50$. (b) Same as (a) for vortex 2. Here, the OW contours corresponding to $Q = -0.024$ (blue) and $Q = -0.10$ (magenta) are selected for advection.

axisymmetric contours of $\lambda_{\pm}$ remain coherent under material advection over the time interval

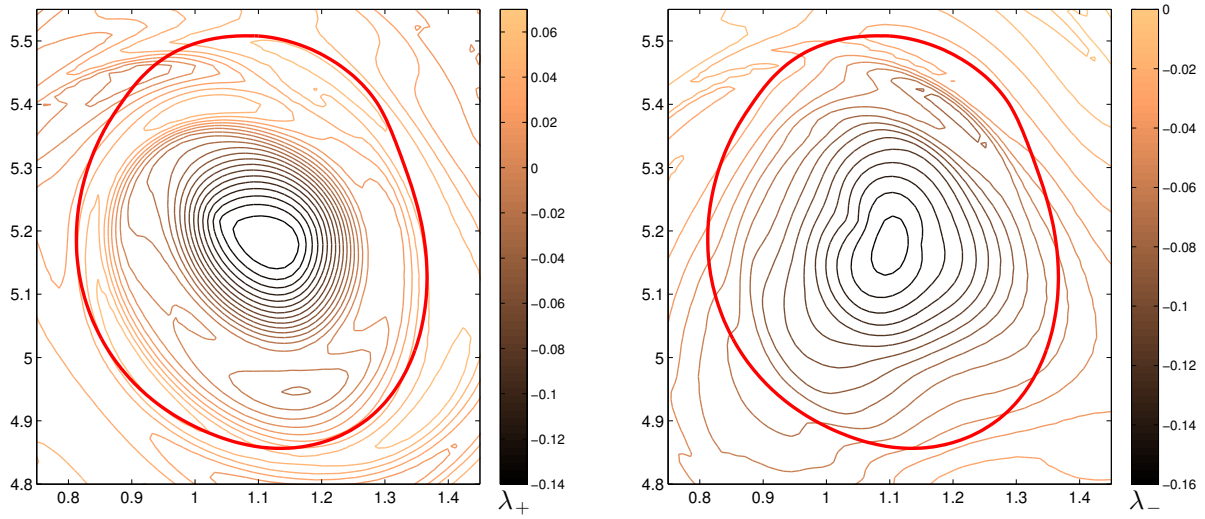

FIG. 11: The contours of λ_+ (left) and λ_- (right) around vortex 1 at time $t = 0$. The Lagrangian vortex boundary is shown with thick red line.

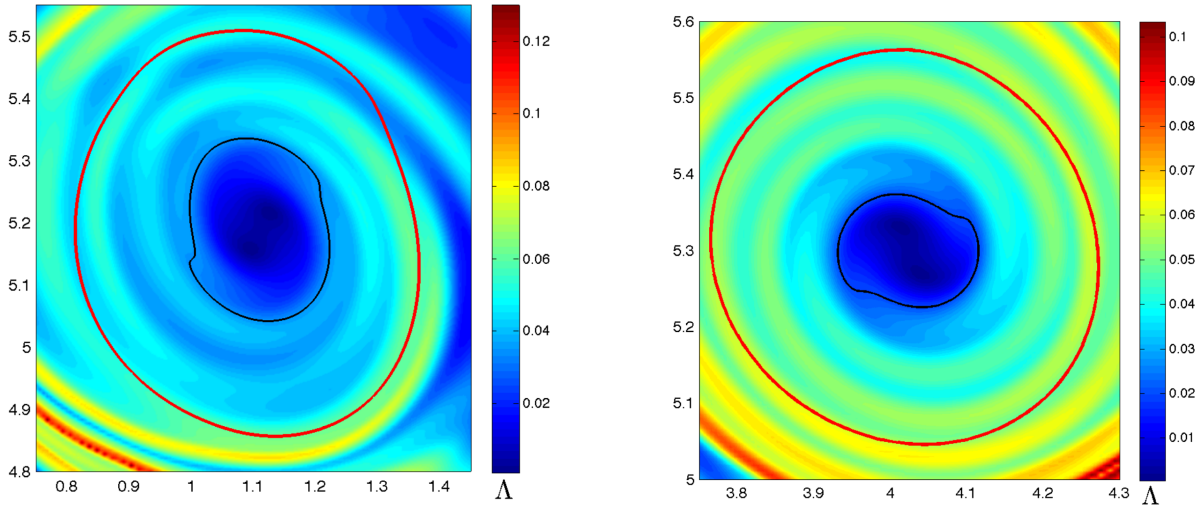

(a) (b)

FIG. 12: (a) Time $t = 0$ position of the Lagrangian vortex boundary (red) for vortex 1. The background color shows the FTLE field. The black curve marks the FTLE contour with $\Lambda = 3.45 \times 10^{-2}$. The FTLE value is chosen such that the corresponding contour is the outermost, almost-axisymmetric contour encircling the vortex core. (b) Same as (a) for vortex 2. Here, the value of the FTLE contour is $\Lambda = 2.0 \times 10^{-2}$

$t \in [0, 50]$. They, however, are significantly smaller (in enclosed surface area) than the true Lagrangian vortex boundary marked by the elliptic LCS.

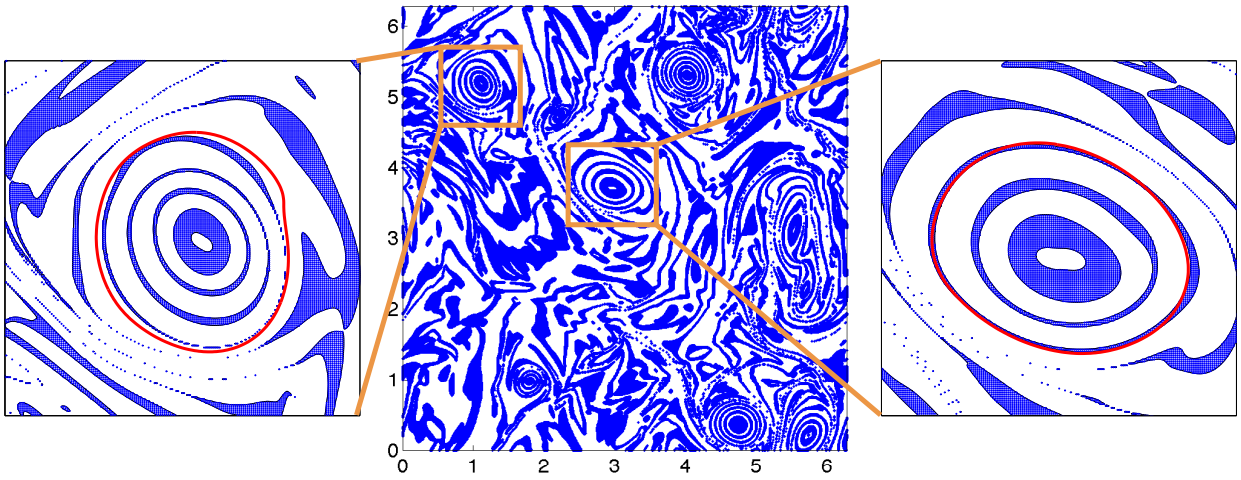

FIG. 13: The mesoelliptic regions (blue) compared to two elliptic LCSs (red).

Compared to the Eulerian criteria, there are far less Lagrangian indicators developed for quantifying coherent vortices. A widely used Lagrangian indicator is the finite-time Lyapunov exponent (FTLE) that measures the maximal local stretching of material lines (Ottino, 1989; Pierrehumbert and Yang, 1993). The FTLE corresponding to a time interval $[a, b]$ is defined as

$$\Lambda(x_a) = \frac{1}{2(b-a)} \log(\lambda_2(x_a)), \tag{9}$$

for any point $x_a \in U$ where λ_2 is the larger eigenvalue of the Cauchy–Green strain tensor C. The FTLE measures the maximum separation of nearby initial conditions over the given time interval. Therefore, its higher values mark regions with high mixing. Conversely, regions with relatively small FTLE values experience less mixing. As a result, one may expect that low-FTLE regions coincide with the coherent vortex regions identified as interiors of the outermost elliptic LCSs.

Figure 12 shows the color-coded FTLE values for vortices 1 and 2. Clearly, the Lagrangian vortex boundary (red curves) cannot be inferred from the FTLE plot. In fact, locally maximal values of FTLE spiral into the Lagrangian vortex boundary, giving the wrong impression that it will stretch significantly under advection.

In addition, FTLE contours around the vortex core lack axisymmetry. The outermost, almost-axisymmetric FTLE contours encircling the vortex cores (black curves) are clearly far from the true vortex boundary marked by the elliptic LCS.

We conclude this section with a comparison between elliptic LCSs and elliptic regions

obtained from the Lagrangian mixing diagnostic of Mezić et al. (2010). This diagnostic classifies a trajectory starting from a point x_a as *mesoellipitic* in an incompressible flow, if the eigenvalues of the deformation gradient $DF(x_a)$ lie on the complex unit circle. Mesoelliptic trajectories are expected to lie in a vortical region. In contrast, if the eigenvalues of $DF(x_a)$ are off the complex unit circle , the trajectory is classified as *mesohyperbolic* and is expected to lie in a strain-dominated region.

Figure 13 shows the mesoelliptic (blue) and mesohyperbolic (white) regions in our turbulent flow. We find that this diagnostic returns both false positives and false negatives in Lagrangian vortex detection. Indeed, a number of mesoelliptic regions appear in non-coherent, hyperbolic mixing regions (compare to figure 7), and substantial portions of each coherent vortex are misclassified as mesohyperbolic (annular white regions). Note that the actual Lagrangian coherent vortex boundaries (i.e., the outermost elliptic LCS) are shadowed by nearby thin mesoelliptic regions. These thin regions, however, occur in concentric families, and we could not establish a systematic a priori criterion for choosing a member of this family as an approximate Lagrangian vortex boundary.

IV. CONCLUSIONS

We have used the variational theory of Haller and Beron-Vera (2013) to detect the boundaries of coherent vortices in a direct numerical simulation of two-dimensional Navier–Stokes turbulence. We demonstrated that these boundaries are optimal in the sense that they are the outermost material lines enclosing a vortex and retaining their shape over long time intervals. They are also frame-independent and Lagrangian by nature.

A comparison with other Eulerian methods (vorticity contours, Okubo-Weiss criterion, λ-parameters) shows that the size of coherent vortices of turbulence is substantially larger than what has been thought before based on Eulerian indicators. At the same time, the actual number of coherent vortices is lower than what is signaled by the same indicators. This is consistent with the findings in Beron-Vera et al. (2013), who observed a similar trend for the ocean eddies in satellite-altimetry-based velocity fields of the South Atlantic. We find that the superfluous vortices suggested by Eulerian indicators are destroyed relatively quickly by the straining induced by repelling and attracting Lagrangian coherent structures present in the flow.

We also compared our results with two Lagrangian indicators: the finite-time Lyapunov exponent (FTLE) and the mesoellipticity of Mezić et al. (2010). The FTLE field indicates the approximate position of vortex cores with a relatively low FTLE value. However, it does not provide an indication of the coherent Lagrangian vortex boundary. As a rule, we have found mesoelliptic regions near the actual coherent Lagrangian vortex boundary. However, we have also identified false positives and false negatives from this diagnostic, which prevented its use in the a priori estimation of Lagrangian vortex boundaries.

Compared to instantaneous Eulerian indicators, such as Okubo-Weiss criterion, our vortex detection is clearly computationally more expensive. It requires accurate advection of a large ensemble of fluid particles, as well as, closed orbit detection in the vector fields (6). Therefore, developing cost effective computational algorithms while staying faithful to the underlying theory is of great interest (see Leung (2011); Shadden (2012); Peikert et al. (2014), for recent developments).

Future theoretical work will focus on the correlation between Lagrangian coherent vortices and the dynamical properties of the flow, e.g., the scale-by-scale transfer of energy and enstrophy (Kelley et al., 2013).

REFERENCES

H. Aref. Stirring by chaotic advection. *J. Fluid Mech.*, 143:1–21, 1984.

V. I. Arnold. *Mathematical Methods of Classical Mechanics*. Springer, 1978.

J. Beem, P. Ehrlich, and K. Easley. Global Lorentzian geometry, volume 202 of monographs and textbooks in pure and applied mathematics, 1996.

F. J. Beron-Vera, Y. Wang, M. J. Olascoaga, G. J. Goni, and G. Haller. Objective detection of oceanic eddies and the Agulhas leakage. *J. of Phys. Oceanogr.*, 43(7), 2013.

G. Boffetta and R. E. Ecke. Two-dimensional turbulence. *Ann. Rev. Fluid Mech.*, 44: 427–451, 2012.

G. Boffetta, A. Celani, S. Musacchio, and M. Vergassola. Intermittency in two-dimensional Ekman–Navier-Stokes turbulence. *Phys. Rev. E*, 66:026304, 2002.

M. S. Chong, A. E. Perry, and B. J. Cantwell. A general classification of three-dimensional flow fields. *Phys. fluids A*, 2(5):765–777, 1990.

J. R. Dormnad and P. J. Prince. A family of embedded Runge-Kutta formulae. *J. Comp.*

Appl. Math., 6:19–26, 1980.

M. Farazmand and G. Haller. Computing Lagrangian Coherent Structures from their variational theory. *Chaos*, 22:013128, 2012.

M. Farazmand and G. Haller. Attracting and repelling Lagrangian coherent structures from a single computation. *Chaos*, 23:023101, 2013.

M. Farazmand, D. Blazevski, and G. Haller. Shearless transport barriers in unsteady two-dimensional flows and maps. *Submitted to Physica D (arXiv preprint arXiv:1308.6136)*, 2013.

U. Frisch. *Turbulence: the legacy of A.N. Kolmogorov*. Cambridge University Press, 1995.

J. Guckenheimer and P. Holmes. *Nonlinear oscillations, dynamical systems, and bifurcations of vector fields*. Springer Verlag, 1983.

A. Hadjighasem, M. Farazmand, and G. Haller. Detecting invariant manifolds, attractors, and generalized KAM tori in aperiodically forced mechanical systems. *Nonlinear Dynamics*, 73(1-2):689–704, 2013.

G. Haller. An objective definition of a vortex. *J. Fluid Mech.*, 525:1–26, 2005.

G. Haller and F. J. Beron-Vera. Geodesic theory of transport barriers in two-dimensional flows. *Physica D*, 241(20):1680 – 1702, 2012.

G. Haller and F. J. Beron-Vera. Coherent Lagrangian vortices: The black holes of turbulence. *J. Fluid Mech.*, 731, R4, 2013.

B. L. Hua and P. Klein. An exact criterion for the stirring properties of nearly two-dimensional turbulence. *Physica D*, 113(1):98–110, 1998.

J. Jeong and F. Hussain. On the identification of a vortex. *J. of Fluid Mech.*, 285:69–94, 1995.

H. Kellay and W. I. Goldburg. Two-dimensional turbulence: a review of some recent experiments. *Reports on Progress in Physics*, 65(5):845, 2002.

D. H. Kelley, M. R. Allshouse, and N. T. Ouellette. Lagrangian coherent structures separate dynamically distinct regions in fluid flows. *Phys. Rev. E*, 88:013017, 2013.

S. Kida and H. Miura. Identification and analysis of vortical structures. *European Journal of Mechanics - B/Fluids*, 17(4):471 – 488, 1998.

R. H. Kraichnan. Inertial ranges in two-dimensional turbulence. *Phys. Fluids*, 10:1417–1423, 1967.

S. Leung. An Eulerian approach for computing the finite time Lyapunov exponent. *J. of*

Comp. Phys., 230(9):3500–3524, 2011.

J. C. McWilliams. The vortices of two-dimensional turbulence. *J. Fluid Mech.*, 219:361–385, 1990.

J. C. McWilliams. *Fundamentals of geophysical fluid dynamics*. Cambridge University Press, 2006.

P. E. Merilees and H. Warn. On energy and enstrophy exchanges in two-dimensional non-divergent flow. *J. Fluid Mech.*, 69:625–630, 1975.

I. Mezić, S. Loire, V. A. Fonoberov, and P. Hogan. A new mixing diagnostic and Gulf oil spill movement. *Science*, 330(6003):486–489, 2010.

A. Okubo. Horizontal dispersion of floatable particles in the vicinity of velocity singularities such as convergences. *Deep Sea Research*, 17:445–454, 1970.

J. M. Ottino. *The Kinematics of mixing: stretching, chaos and transport*. Cambridge University Press, 1989.

R. Peikert, A. Pobitzer, F. Sadlo, and B. Schindler. A comparison of finite-time and finite-size Lyapunov exponents. *Topological Methods in Data Analysis and Visualization III. Springer*, 2014.

R. T. Pierrehumbert and H. Yang. Global chaotic mixing on isentropic surfaces. *J. Atmos. Sci.*, 50:2462–2480, 1993.

S. C Shadden. Lagrangian coherent structures. *Transport and Mixing in Laminar Flows: From Microfluidics to Oceanic Currents*, pages 59–89, 2012.

M. Tabor and I. Klapper. Stretching and alignment in chaotic and turbulent flows. *Chaos, Solitons & Fractals*, 4(6):1031 – 1055, 1994.

C. Truesdell and W. Noll. *The non-linear field theories of mechanics*. Springer, New York, third edition, 2004.

Y.-K. Tsang, E. Ott, T. M. Antonsen, and P. N. Guzdar. Intermittency in two-dimensional turbulence with drag. *Phys. Rev. E*, 71:066313, 2005.

J. Weiss. The dynamics of enstrophy transfer in two-dimensional hydrodynamics. *Physica D*, 48:273–294, 1991.